ARTICLE

Architecture of Pd–Au Bimetallic Nanoparticles in Sodium Bis(2-ethylhexyl)sulfosuccinate Reverse Micelles As Investigated by X-ray Absorption Spectroscopy

Ching-Hsiang Chen,[†,§] Loka Subramanyam Sarma,[†] Jium-Ming Chen,[†] Shou-Chu Shih,[†] Guo-Rung Wang,[†] Din-Goa Liu,[‡] Mau-Tsu Tang,[‡] Jyh-Fu Lee,[‡] and Bing-Joe Hwang[†,‡,*]

[†]Nanoelectrochemistry Laboratory, Department of Chemical Engineering, National Taiwan University of Science and Technology, Taipei 106, Taiwan, [‡]National Synchrotron Radiation Research Center, Hsinchu 300, Taiwan, and [§]Institute of Atomic and Molecular Sciences, Academia Sinica, Taipei 115, Taiwan

ABSTRACT In this study, we demonstrate the unique application of X-ray absorption spectroscopy (XAS) as a fundamental characterization tool to help in designing and controlling the architecture of Pd–Au bimetallic nanoparticles within a water-in-oil microemulsion system of water/sodium bis(2-ethylhexyl)sulfosuccinate (AOT)/*n*-heptane. Structural insights obtained from the *in situ* XAS measurements recorded at each step during the formation process revealed that Pd–Au bimetallic clusters with various Pd–Au atomic stackings are formed by properly performing hydrazine reduction and redox transmetalation reactions sequentially within water-in-oil microemulsions. A structural model is provided to explain reasonably each reaction step and to give detailed insight into the nucleation and growth mechanism of Pd–Au bimetallic clusters. The combination of *in situ* XAS analysis at both the Pd K-edge and the Au L_{III}-edge and UV–vis absorption spectral features confirms that the formation of Pd–Au bimetallic clusters follows a $(Pd_{nuclei}–Au_{stack})–Pd_{surf}$ stacking. This result further implies that the thickness of Au_{stack} and Pd_{surf} layers may be modulated by varying the dosage of the Au precursor and hydrazine, respectively. In addition, a bimetallic $(Pd–Au)_{alloy}$ nanocluster with a $(Pd_{nuclei}–Au_{stack})–(Pd–Au_{alloy})_{surf}$ stacking was also designed and synthesized in order to check the feasibility of Pd_{surf} layer modification. The result reveals that the Pd_{surf} layer of the stacked $(Pd_{nuclei}–Au)_{stack}$ bimetallic clusters can be successfully modified to form a $(Au–Pd\ alloy)_{surf}$ layer by a co-reduction of Pd and Au ions by hydrazine. Further, we demonstrate the alloying extent or atomic distribution of Pd and Au in Pd–Au bimetallic nanoparticles from the derived XAS structural parameters. The complete XAS-based methodology, demonstrated here on the Pd–Au bimetallic system, can easily be extended to design and control the alloying extent or atomic distribution, atomic stacking, and electronic structure to construct many other types of bimetallic systems for interesting applications.

KEYWORDS: bimetallic nanoparticles · X-ray absorption spectroscopy · redox transmetalation reaction · reverse micelles · atomic distribution

*Address correspondence to bjh@mail.ntust.edu.tw.

Received for review April 30, 2007 and accepted July 31, 2007.

Published online August 25, 2007.
10.1021/nn700021x CCC: $37.00

Bimetallic nanoparticles (NPs) in the form of either alloys or core–shell nanostructures are of great interest[1] from both scientific and technological perspectives because of their attractive physical and chemical properties, resulting from not only size effects but also the combination of different metals.[2,3] It was observed that the activity and selectivity of the metal catalysts can be drastically influenced by the presence of a second metal component.[4] The "ligand effect", which refers to the electronic structure modifications resulting from the addition of one metal to a second metal, leads to the formation of heterometallic bonds involving either charge transfer between the metals or orbital rehybridization of the metals. These changes can alter the properties of the mixed-metal system, and various bimetallic systems formed accordingly have been reported.[5–7] Among the various bimetallic nanoclusters (NCs), Pd–Au has been widely explored as a catalytic material for a variety of reactions, including vinyl acetate synthesis,[8–10] hydrodesulfurization of thiophene,[11] acetylene hydrogenation,[12] and oxidation of alcohols to aldehydes.[13] Most of the numerous recent reports have focused on the synthesis and catalytic applications of Pd–Au bimetallic NCs.[14–19] Although significant contributions have been devoted to the synthesis and characterization of Pd–Au bimetallic clusters, the atomic distribution of the NCs, structural dynamics, and thermodynamic behavior, which are the key parameters for catalyst design and architecture, remain less explored.

We have recently reported that the properties of bimetallic catalysts can be significantly influenced by the extent of alloying between the two constituent elements, based on X-ray absorption spectroscopy (XAS) methodology.[20] In order to control properties such as atomic distribution, stacking order, and surface composition, which are crucial for the architecture of bimetallic NPs with tailored structure and functions, understanding the formation mechanism remains a major scientific interest. The commonly available X-ray diffraction (XRD) technique provides information about the long-range or-

dering and periodicities, preferably of single crystals or polycrystals, and lacks the means to identify short-range ordering information; hence, conclusions about the alloy structure of nanosized particles cannot be drawn simply from XRD. In fact, it seems that anomalous wide-angle X-ray scattering is able to give the same information on the distribution of the two metals inside bimetallic clusters.[21] Techniques like transmission electron microscopy (TEM) and high-resolution (HR) TEM provide only a qualitative understanding of the structure of bimetallic NPs. For example, the HRTEM method enables one to distinguish the core–shell structure on the basis of observing different lattice spacing. On the other hand, TEM emphasizes the intensity contrast in understanding the structure of bimetallic NPs. One method suitable for the study of the structure of metal clusters is *in situ* XAS, comprising both X-ray absorption near-edge spectroscopy (XANES) and extended X-ray absorption fine structure spectroscopy (EXAFS) regions.[22,23] XANES can reveal the oxidation state and d-band occupancy of a specific atom, as well as the size of metallic clusters,[24,25] while EXAFS provides a powerful tool for the analysis of local atomic structure, giving accurate information about the average local atomic environment. EXAFS is particularly sensitive to interatomic distances and local disorder and has been successfully utilized to resolve subtle structural details about NPs.[26] XAS has been proved as a powerful technique for the characterization of bimetallic catalysts,[27–29] since it is difficult to obtain structural information on such systems by conventional material analysis methods at the early stages.

We have recently made some significant contributions that highlight the applicability of XAS to study nanoparticle formation mechanisms.[30–33] We also applied XAS to study the chemical transformation of bimetallic NPs to ternary metallic NPs by a cation redox reaction.[34] In this study, we further advance the applicability of XAS to design and construct Pd–Au bimetallic NPs with various Pd–Au atomic stackings in water-in-oil microemulsions by properly employing hydrazine reduction reactions (HRRs) together with redox transmetalation reactions (RTMs). In a RTM process, the sacrificial oxidation of one metal results in the deposition of another metal ion to produce bimetallic NPs.[35] The thickness of the gold and palladium layers and their surface composition can be controlled by adjusting the dosage of the gold precursors and the reducing agent, respectively. We know that ethylene dehydrogenation can be catalyzed by a Pd cluster, especially on the surface of Pd(111) and Pd(100) planes.[36,37] It was reported that the addition of Au to Pd clusters can lead to an enhancement of ethylene dehydrogenation[38] due to the sp- and d-band charge redistribution or orbital hybridization, indicating that controlling the atomic ratio N_{Au}/N_{Pd} would further control the electronic perturbation of Au and Pd. We also attempted to provide details on the atomic distribution and structural insights into Au–Pd bimetallic clusters, since the catalytic activity of bimetallic clusters is strongly influenced by their atomic distribution and structure. Furthermore, after getting detailed knowledge of the reaction mechanism, we tried to design a $(Pd–Au)_{alloy}$ bimetallic NP with three stacking regions, *viz.*, $(Pd_{nuclei}–Au)_{stack}–(Au–Pd\ alloy)_{surf}$, by controlling two HRRs and one RTM. It is believed that the detailed knowledge about the formation mechanism gained from *in situ* XAS in this study can be further utilized to design and modify the alloying extent, atomic distribution, stacking order, and electronic configuration of other bimetallic NPs for interesting applications.

RESULTS AND DISCUSSION

***In Situ* XANES at Various Stages in the Formation of Bimetallic Pd–Au Clusters with Various Atomic Stackings.** XANES can provide information on the electronic transition from the core level to the vacant d states of the absorbing atom and is recognized as a powerful tool to characterize *in situ* d-electron configuration in catalysts. The Pd K-edge XANES spectrum is recorded for the microemulsion system containing Pd^{2+} ions as a function of dosage of reducing agent, hydrazine (N_2H_5OH), in the hydrazine reduction reactions and as a function of N_{Au}/N_{Pd} ratio in the redox transmetalation reactions. The corresponding Pd K-edge XANES spectra of Pd–Au bimetallic nanoparticles with various stackings are shown in Figure 1.

In the Pd K-edge XANES spectra, the absorption transition in the pre-edge region is a 1 s to 4 d dipole-forbidden transition according to the selection rule, $\Delta l = 1$ and $\Delta j = 1$, where l and j are orbital angular momentum and total angular moment of the local density of states, respectively.[39] The absorption threshold resonance, called a white line, appearing between 24360 and 24380 eV, corresponds to the electronic transitions that arise from the 1 s to unoccupied 4 p states above the Fermi level. The second (24385 eV) and third (24435 eV) peaks are attributed to 1 s $\rightarrow$ dp and 1 s $\rightarrow$ dsp transitions, respectively. This white line intensity is sensitive to the change in electron occupancy of the valance orbital and ligand field environments of an absorber.[40] For this reason, it can be used to estimate the density of the unoccupied states and the changes in the oxidation state of the Pd absorber. The energy shift can also be related to a change in the effective number of valence electrons at the absorbing site. As can be seen from Figure 1, the edge energy of the initial Pd^{2+} solution gradually shifts toward the reference Pd foil, with an increase in the amount of reducing agent from 0 to 44×10^{-5} mol, indicating the progressive reduction of Pd^{2+} to Pd^0 (Pd_{nuclei} NPs). For a better understanding, we also provide more detailed Pd K-edge XANES spectra, recorded during the formation of Pd–Au bimetallic NPs, in the Supporting Information, in which a gradual decrease in white line intensity can also be observed with increasing amount of reducing agent from 0 to 44×10^{-5} mol (Figure 1S). After the formation of Pd clusters, the Au precursor solution, *i.e.*, the $HAuCl_4$ emulsion, was introduced, and the hydrazine dosage was increased before the HRRs were performed. The stability of the state of the system was checked by com-

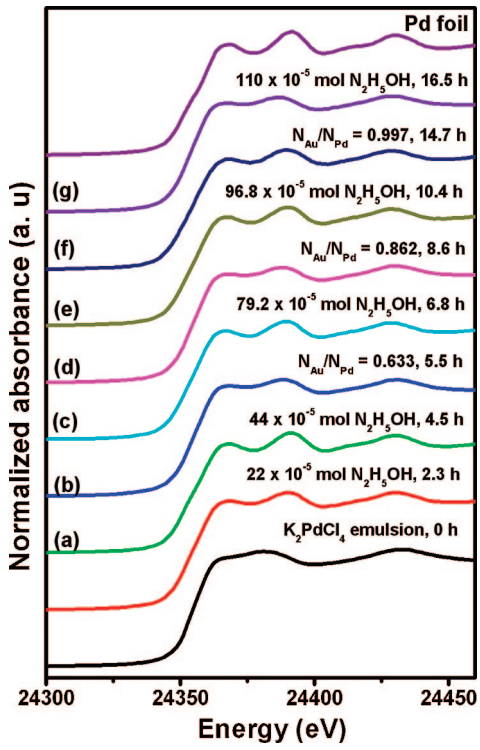

Figure 1. Normalized XANES spectra near the Pd K-edge at various steps during the formation of Pd–Au bimetallic clusters with various atomic stacking in reverse micelles, with K_2PdCl_4 and Pd foil as references: (a) Pd_{nuclei}, (b) (Pd_{nuclei}–$Au_{stack\text{-}1}$), (c) (Pd_{nuclei}–$Au_{stack\text{-}1}$)–Pd_{surf}, (d) (Pd_{nuclei}–$Au_{stack\text{-}2}$), (e) (Pd_{nuclei}–$Au_{stack\text{-}2}$)–Pd_{surf}, (f) (Pd_{nuclei}–$Au_{stack\text{-}3}$), and (g) (Pd_{nuclei}–$Au_{stack\text{-}3}$)–Pd_{surf} NPs.

paring two sequential X-ray absorption spectra before proceeding to the next stage.

After the addition of the Au^{3+} precursor (stoichiometric ratio $N_{Au}/N_{Pd} = 0.633$) at 5.5 h (Pd_{nuclei}–$Au_{stack\text{-}1}$ NPs), the white line intensity increases slightly due to the oxidation of part of the Pd_{nuclei} NPs. The edge energy is positioned more closely to the K_2PdCl_4 microemulsion, indicating the formation of Pd–Cl species at this stage, which will be further confirmed during the discussion of EXAFS results. After the addition of 79.2×10^{-5} mol of hydrazine at 6.8 h, the edge position approaches the reference Pd foil, indicating the reduction of these $PdCl_4^{2-}$ species back to Pd^0 ((Pd_{nuclei}–$Au_{stack\text{-}1}$)–Pd_{surf} NPs). The edge shift to K_2PdCl_4 during the formation of (Pd_{nuclei}–$Au_{stack\text{-}2}$) and (Pd_{nuclei}–$Au_{stack\text{-}3}$) NPs by RTMs is consistent with the oxidation of Pd clusters, whereas the edge shift toward the reference Pd during the formation of (Pd_{nuclei}–$Au_{stack\text{-}2}$)–Pd_{surf} and (Pd_{nuclei}–$Au_{stack\text{-}3}$)–Pd_{surf} NPs by HRRs indicates the reduction of Pd^{2+} ions.

The Au L_{III}-edge XANES spectra of the bimetallic Au–Pd microemulsion system are shown in Figure 2. The white line intensity of $HAuCl_4$, which is positioned around 11923 eV,[41] *i.e.*, 4 eV above the edge of the Au L_{III}-edge, is sharply decreased and matched well with the magnitude of white line intensity of the reference Au foil soon after the $HAuCl_4$ microemulsion is introduced into the Pd microemulsion complex containing Pd clusters at 6.0 h. This observation indicates that Au^{3+}

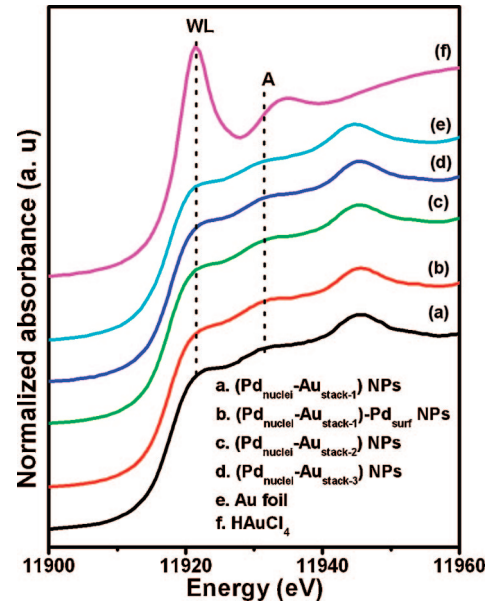

Figure 2. Normalized XANES spectra near the Au L_{III}-edge at various steps during the formation of Pd–Au bimetallic clusters with various atomic stacking in reverse micelles, $HAuCl_4$, and reference Au foil.

ions are reduced to Au^0 after interacting with Pd clusters. The white line intensity in the Au L_{III}-edge XANES spectra shows no change, but the intensity of peak A increases slightly, indicating the possibility of a new interaction between Au and Pd atoms after the addition of 79.2×10^{-5} mol of hydrazine during the formation of (Pd_{nuclei}–$Au_{stack\text{-}1}$)–Pd_{surf} NPs. When the ratio of N_{Au}/N_{Pd} is increased to 0.862 (Pd_{nuclei}–$Au_{stack\text{-}2}$ NPs), the white line intensity is not changed when compared to the white line intensity of Pd_{nuclei}–$Au_{stack\text{-}1}$ NPs, whereas the intensity of peak A is lowered, indicating a discernible difference in the d-bands of the Au core holes. It would further imply that the electronic configurations of clusters formed at these two stoichiometric ratios are different. Further increase in the N_{Au}/N_{Pd} ratio to 0.997 does not change the white line intensity, indicating that all the Au^{3+} ions are reduced to Au^0 during the formation of Pd_{nuclei}–$Au_{stack\text{-}3}$ NPs.

***In Situ* EXAFS at Various Stages in the Formation of Bimetallic Pd–Au Clusters with Various Atomic Stackings.** The Fourier-transformed (FT) k^3-weighted EXAFS spectra ($\Delta k = 4.05$–14.10 Å^{-1}) of the microemulsion system at various HRRs and RTMs are shown in Figure 3. As can be seen from Figure 3, the K_2PdCl_4 emulsion exhibits a peak between 1.5 and 2.0 Å, corresponding to a Pd–Cl bond. After the addition of 22×10^{-5} mol of N_2H_5OH at 2.3 h, the magnitude of Pd–Cl bond is decreased, and a new peak appears between 2.0 and 3.0 Å, attributed to a Pd–Pd bond, indicating that $PdCl_4^{2-}$ ions are reduced and Pd clusters are formed directly without any intermediate. The corresponding chemical reaction can be written as shown in eq 1.

$$N_2H_5OH + PdCl_4^{2-} + 2H^+ \rightarrow N_2 + H_2 + Pd^0 + 4HCl + H_2O \quad (1)$$

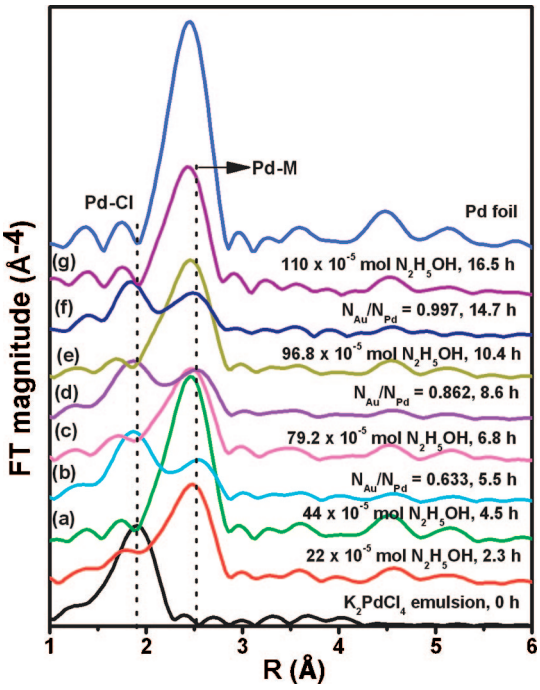

Figure 3. FT-EXAFS spectra obtained at the Pd K-edge at various stages in the formation of bimetallic Pd–Au NPs with various atomic stackings and reference Pd foil: (a) Pd_{nuclei}, (b) (Pd_{nuclei}–$Au_{stack\text{-}1}$), (c) (Pd_{nuclei}–$Au_{stack\text{-}1}$)–Pd_{surf}, (d) (Pd_{nuclei}–$Au_{stack\text{-}2}$), (e) (Pd_{nuclei}–$Au_{stack\text{-}2}$)–Pd_{surf}, (f) (Pd_{nuclei}–$Au_{stack\text{-}3}$), and (g) (Pd_{nuclei}–$Au_{stack\text{-}3}$)–Pd_{surf} NPs.

After the addition of 44×10^{-5} mol of N_2H_5OH at 4.5 h, the FT peak corresponding to the Pd–Cl bond disappears completely, and the magnitude of the Pd–Pd bond increases. This implies that all of the palladium ions are completely reduced to Pd^0 and transformed to Pd clusters (Pd_{nuclei} NPs). After the addition of the Au^{3+} emulsion at 5.5 h ($N_{Au}/N_{Pd} = 0.633$), the magnitude of the Pd–Pd bond is decreased and shifted slightly to higher R values due to the presence of Au. A peak corresponding to a Pd–Cl bond, which has a magnitude slightly less than that of the equivalent peak in the EXAFS spectrum of the $PdCl_4^{2-}$ precursor, appears between 1.5 and 2.0 Å, indicating that the oxidation of Pd clusters takes place during the redox transmetalation process (Pd_{nuclei}–$Au_{stack\text{-}1}$ NPs).

The appearance of the Pd–Cl bond is consistent with our previous study, in which we showed that the reaction between monometallic Pd clusters with the microemulsion containing Pt^{4+} ions generated the Pd–Cl bond due to the oxidation of Pd clusters.[33] By increasing the total amount of hydrazine to 79.2×10^{-5} mol at 6.8 h ((Pd_{nuclei}–$Au_{stack\text{-}1}$)–Pd_{surf} NPs), the magnitude of the Pd–Cl bond is decreased, and a new broad peak attributed to a Pd–M bond is formed. The FEFF7 software package was used to fit the Pd–Pd and Pd–Au bonds, as shown in Table 1. After further addition of the Au precursor ($N_{Au}/N_{Pd} = 0.862$) at 8.6 h (Pd_{nuclei}–$Au_{stack\text{-}2}$ NPs), the magnitude of the broad peak of the Pd–M bond decreases, whereas the magnitude of the Pd–Cl bond increases. Upon addition of the reducing agent to 96.8×10^{-5} mol at 10.4 h ((Pd_{nuclei}–$Au_{stack\text{-}2}$)–Pd_{surf} NPs), the magnitude of not only the Pd–Pd bond but also the Pd–Au bond is increased, and the peak corresponding to the Pd–Cl is eliminated. After equilibrium is reached at 14.7 h, further Au precursor is added to make equal the atomic ratio between the Pd and Au atoms (Pd_{nuclei}–$Au_{stack\text{-}3}$ NPs). A similar phenomenon is observed in the first and second additions of the Au precursors. After addition of reducing agent to 110×10^{-5} mol at 16.5 h ((Pd_{nuclei}–$Au_{stack\text{-}3}$)–Pd_{surf} NPs), the contribution from Pd–Cl bonding completely disappears.

The FT k^3-weighted EXAFS spectra ($\Delta k = 3.39$–13.25 Å^{-1}) obtained at the Au L_{III}-edge of the bimetallic Pd–Au microemulsion system are shown in Figure 4. It is found that the feature of the Fourier transform spectra of the Au absorber for various atomic ratios N_{Au}/N_{Pd} (for the NPs obtained during all the RTMs, *i.e.*, Pd_{nuclei}–$Au_{stack\text{-}1}$, Pd_{nuclei}–$Au_{stack\text{-}2}$, and Pd_{nuclei}–$Au_{stack\text{-}3}$) exhibits two bonds between 1.5 and 3.5 Å in length, the magnitude of which is increasing with the Au stacking. After fitting of the k^3-weighted EXAFS data by using the FEFF7 software package, the two bonds are evaluated as the Au–Pd and Au–Au bonds, respectively. As can be seen in Figure 4, the Au–Cl bond is not found during all the RTMs, and the figure shows only the Au–metal bonds after the addition of the Au precursors, indicating that all of the $AuCl_4^-$ ions are reduced completely *via* RTM. The structural parameters (coordination number N, bond distance R, Debye–Waller factor σ^2, and inner potential shift ΔE_0) derived from the Au L_{III}-edge EXAFS data analysis of Pd–Au bimetallic system are shown in Table 2. The results of Pd K-edge

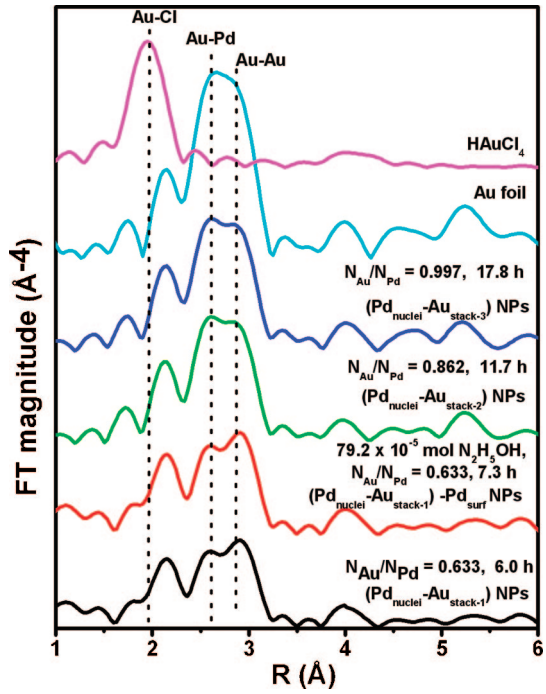

Figure 4. FT-EXAFS spectra obtained at the Au L_{III}-edge at various stages of bimetallic Pd–Au NPs formation in sodium bis(2-ethylhexyl)sulfosuccinate (AOT) reverse micelles at various N_{Au}/N_{Pd} ratios, as a function of reducing agent dosage, and reference compounds $HAuCl_4$ and Au foil.

TABLE 1. Structural Parameters Derived from the Pd K-Edge EXAFS Data Analysis at Various Stages in the Formation of Pd–Au Bimetallic Clusters with Various Atomic Stackings and the Reference Pd Foil[a]

reaction state	amount of N_2H_5OH (mol)	time (h)	atomic ratio (N_{Au}/N_{Pd})	shell	N	R_j (Å)	σ^2 ($\times 10^{-3}$ Å^2)	ΔE_0 (eV)	R factor
	0	0	0	Pd–Cl	4.00 (0.13)	2.320 (0.003)	4.8 (0.3)	4.5 (0.3)	0.0089
	22×10^{-5}	2.3	0	Pd–Cl Pd–Pd	1.86 (0.12) 6.61 (0.08)	2.329 (0.003) 2.743 (0.002)	8.9 (0.1) 7.8 (0.1)	6.9 (0.4) −1.1 (0.1)	0.0021
Pd_{nuclei}	44×10^{-5}	4.5	0	Pd–Pd	8.90 (0.06)	2.742 (0.001)	6.8 (0.3)	−1.4 (0.3)	0.0022
Pd_{nuclei}–$Au_{stack\text{-}1}$ NPs		5.5	0.633	Pd–Cl Pd–Pd Pd–Au	2.84 (0.13) 2.17 (0.08) 0.21 (0.08)	2.314 (0.003) 2.742 (0.002) 2.757 (0.003)	4.8 (0.2) 8.4 (0.1) 0.0 (0.2)	1.2 (0.5) −4.1 (0.3) 13.0 (0.8)	0.0036
(Pd_{nuclei}–$Au_{stack\ 1}$)–Pd_{surf} NPs	79.2×10^{-5}	6.8		Pd–Pd Pd–Au	6.37 (0.11) 0.87 (0.07)	2.749 (0.004) 2.755 (0.002)	7.5 (0.3) 5.6 (0.3)	−3.9 (0.2) 0.1 (0.3)	0.0196
Pd_{nuclei}–$Au_{stack\text{-}2}$ NPs		8.6	0.862	Pd–Cl Pd–Pd Pd–Au	2.53 (0.13) 2.59 (0.06) 0.24 (0.09)	2.313 (0.003) 2.742 (0.002) 2.757 (0.002)	5.3 (0.3) 5.9 (0.2) 0.0 (0.2)	0.1 (0.6) −5.1 (0.2) 12.1 (0.5)	0.0033
(Pd_{nuclei}–$Au_{stack\text{-}2}$)–Pd_{surf} NPs	96.8×10^{-5}	10.4		Pd–Pd Pd–Au	6.46 (0.07) 1.06 (0.08)	2.749 (0.002) 2.755 (0.004)	6.3 (0.1) 4.3 (0.2)	−2.8 (0.3) 0.9 (0.2)	0.0083
Pd_{nuclei}–$Au_{stack\text{-}3}$ NPs		14.7	0.997	Pd–Cl Pd–Pd Pd–Au	1.96 (0.14) 1.81 (0.07) 0.21 (0.09)	2.310 (0.003) 2.742 (0.002) 2.757 (0.002)	4.1 (0.3) 4.4 (0.1) 0.0 (0.3)	−0.3 (0.5) −7.4 (0.3) 3.3 (0.6)	0.0083
(Pd_{nuclei}–$Au_{stack\text{-}3}$)–Pd_{surf} NPs	110×10^{-5}	16.5		Pd–Pd Pd–Au	5.67 (0.06) 1.09 (0.08)	2.741 (0.002) 2.755 (0.002)	5.4 (0.2) 4.4 (0.2)	−3.3 (0.2) −2.6 (0.1)	0.0081
(Pd_{nuclei}–$Au_{stack\text{-}1}$)–(Pd–Au_{alloy})$_{surf}$ NPs	110×10^{-5}		1.000	Pd–Pd Pd–Au	1.91 (0.13) 4.12 (0.07)	2.744 (0.003) 2.794 (0.002)	4.4 (0.3) 5.5 (0.2)	−3.9 (0.2) −7.6 (0.6)	0.0292
Pd foil				Pd–Pd	12.00 (0.12)	2.748 (0.004)	6.4 (0.5)	2.5 (0.3)	0.0043

[a] N, coordination number; R_j, coordination distance; σ^2, Debye–Waller factor; ΔE_0, inner potential correction.

FT-EXAFS data analysis disclosed that Pd ions are completely reduced in all the HRRs, and the Au L_{III}-edge FT-EXAFS data results revealed that Au ions are completely reduced during all the RTMs.

The k^3-weighted EXAFS oscillations at the Pd K-edge recorded for (Pd_{nuclei}–$Au_{stack\text{-}1}$)–Pd_{surf}, (Pd_{nuclei}–$Au_{stack\text{-}2}$)–Pd_{surf}, and (Pd_{nuclei}–$Au_{stack\text{-}3}$)–Pd_{surf} NPs formed during HRRs, and at the Au L_{III}-edge recorded for Pd_{nuclei}–$Au_{stack\text{-}1}$, Pd_{nuclei}–$Au_{stack\text{-}2}$, and Pd_{nuclei}–$Au_{stack\text{-}3}$ NPs formed during RTMs, are shown in Figures 5 and 6, respectively. The EXAFS oscillation frequencies and the features of the curves at both the Pd K-edge and the Au L_{III}-edge of each state are different from those of Pd and Au foils, especially in the high-k region, indicating the existence of a correlation between Pd and Au. All these observations indicate that the metallic ions are reduced and the Pd–Au bimetallic clusters are formed in each state.

The reliability of the XAS data obtained at all the stages in the formation of Pd–Au bimetallic clusters is checked by comparing the FEFF7 theoretical fit with the back-transformed experimental EXAFS data obtained at the Pd K-edge and the Au L_{III}-edge. However, we have shown the fitting data only for the bimetallic Pd–Au clusters with various atomic stackings, *i.e.*, (Pd_{nuclei}–$Au_{stack\text{-}1}$)–Pd_{surf}, (Pd_{nuclei}–$Au_{stack\text{-}2}$)–Pd_{surf}, and (Pd_{nuclei}–$Au_{stack\text{-}3}$)–Pd_{surf} NPs formed at the three atomic ratios (N_{Au}/N_{Pd}) 0.633, 0.862, and 0.997, respectively. The two-shell theoretical fit matches closely with the back-transformed experimental data (shown as open circles and solid squares, respectively, in Figures 2S and 3S in the Supporting Information), indicating satisfactory fitting for not only the Pd–Au and Pd–Pd bonds but also the Au–Pd and Au–Au bonds.

Architecture and Formation of Bimetallic Pd–Au Bimetallic Nanoparticles in AOT Reverse Microemulsions. In this section we will discuss the structural details that are obtained fromthe XAS parameters obtained at the Pd K-edge and the Au L_{III}-edge, shown in Tables 1 and 2, respectively. A schematic representation of the architecture of Pd–Au bimetallic NPs formed at various stages is shown in Scheme 1.

HRR-1. The coordination number N_{Pd-Cl} of the K_2PdCl_4 emulsion is found to be 4.00 in the absence of reducing agent. After the addition of 22×10^{-5} mol of N_2H_5OH at 2.3 h, N_{Pd-Cl} is decreased to 1.86, and contribution from Pd coordination begins to appear (N_{Pd-Pd}, 6.61), indicating the formation of Pd nuclei through the HRR enhanced by an intermicellar exchange process.[42] The reduction of metal ions within the cores of reverse micelles can result in the growth of nano-sized metal particles.[30–33] This particle growth within the cores of the reverse micelles depends strongly on the exchange of the reactants between micelles. As can be seen, further increasing the hydrazine dosage to 44×10^{-5} mol at 4.5 h leads to a complete absence of Pd–Cl coordination and an increase in Pd–Pd coordination, indicating the growth of Pd_{nuclei} clusters (see **HRR-1**, Scheme 1). The coordination number derived from XAS is a strong and nonlinear function of the particle diameter up to 3–5 nm. This property has been widely used in EXAFS analysis to determine the particle size.[26]

TABLE 2. Structural Parameters Derived from the Au L_{III}-Edge EXAFS Data Analysis at Various Stages in the Formation of Pd–Au Bimetallic Clusters with Various Atomic Stackings and the Reference Au Foil[a]

reaction state	amount of N_2H_5OH (mol)	time (h)	atomic ratio (N_{Au}/N_{Pd})	shell	N	R_j (Å)	σ^2 ($\times 10^{-3}$ Å^2)	ΔE_0 (eV)	R factor
Pd_{nuclei}–$Au_{stack\text{-}1}$ NPs		6.0	0.633	Au–Pd	1.05 (0.12)	2.755 (0.002)	11.3 (0.7)	−4.6 (0.8)	0.0154
				Au–Au	7.95 (0.12)	2.855 (0.003)	8.7 (0.3)	2.7 (0.2)	
(Pd_{nuclei}–$Au_{stack\text{-}1}$)–Pd_{surf} NPs	79.2×10^{-5}	7.3		Au–Pd	1.37 (0.14)	2.755 (0.003)	10.2 (0.8)	−4.6 (0.7)	0.0196
				Au–Au	8.17 (0.14)	2.855 (0.004)	9.5 (0.4)	2.9 (0.5)	
Pd_{nuclei}–$Au_{stack\text{-}2}$ NPs		11.7	0.862	Au–Pd	1.25 (0.11)	2.755 (0.002)	14.8 (0.5)	−4.6 (0.7)	0.0083
				Au–Au	8.45 (0.09)	2.855 (0.003)	8.2 (0.3)	2.0 (0.2)	
Pd_{nuclei}–$Au_{stack\text{-}3}$ NPs		17.8	0.997	Au–Pd	1.10 (0.09)	2.755 (0.001)	14.7 (0.6)	−4.6 (0.7)	0.0081
				Au–Au	9.20 (0.10)	2.856 (0.004)	8.4 (0.2)	2.1 (0.2)	
(Pd_{nuclei}–$Au_{stack\text{-}1}$)–$(PdAu)_{alloy}$ NPs	110×10^{-5}		1.000	Au–Pd	4.12 (0.15)	2.794 (0.003)	0.5 (0.2)	7.4 (0.5)	0.0292
				Au–Au	6.41 (0.09)	2.822 (0.004)	3.1 (0.3)	10.8 (0.3)	
Au foil				Au–Au	12.00 (0.15)	2.865 (0.005)	8.4 (0.5)	1.1 (0.4)	0.0120

[a]Notation as in Table 1.

The Pd–Pd coordination number of Pd_{nuclei} clusters is found to be 8.9, indicating that the diameter of Pd clusters is between 1.5 and 2.0 nm.

RTM-1. After the addition of a $AuCl_4^-$ emulsion to the microemulsion containing Pd clusters, the N_{Pd-Cl}, N_{Pd-Pd}, and N_{Pd-Au} are found to be 2.84, 2.17, and 0.21, respectively ($N_{Au}/N_{Pd} = 0.633$). The decrease in N_{Pd-Pd} coordination and increase in N_{Pd-Cl} coordination suggests the sacrificial oxidation of Pd clusters upon interaction with Au^{3+} ions, and the appearance of N_{Pd-Au} indicates the deposition of Au on the Pd surface *via* a redox transmetalation process to form Pd_{nuclei}–$Au_{stack\text{-}1}$ NPs with a first Au stacking (**RTM-1**, Scheme 1). As two kinds of chemical species, $PdCl_4^{2-}$ and Pd–Au clusters, with three kinds of chemical bonds, Pd–Cl, Pd–Pd, and Pd–Au, dispersed in the solution a three-shell model are used to fit the k^3-weighted EXAFS data of the Pd K-edge, the real coordination number is underestimated due to the fact that all the coordination numbers of the Pd–Cl, Pd–Pd, and Pd–Au are averaged out, since XAS is an averaging technique. This implies not only that the coordination number of the Pd–Au bond should be larger than 0.21 but also that the coordination number of the Pd–Cl bond should be larger than 2.84 at this stage. The higher coordination of the Pd–Cl bond indicates that most of the Pd clusters are dissolved and form $PdCl_4^{2-}$ species. At this stage, we strongly believe that the electrons required for the reduction of Au^{3+} ions come mainly from the oxidation of Pd clusters and not from the oxidation of hydrazine. Most of the hydrazine is consumed during the Pd cluster formation. The amount of residual hydrazine present in the system is 3×10^{-5} mol, corresponding to a molar ratio of $[N_2H_5OH]/[Au^{3+}]$ of 0.07:1, far below the amount required to reduce Au^{3+} ions.[43] Besides, due to the instability of hydrazine, the amount of residual hydrazine should be much less than 3×10^{-5} mol. Hence, we believe that residual hydrazine, if present, is not sufficient to reduce Au^{3+} ions. The

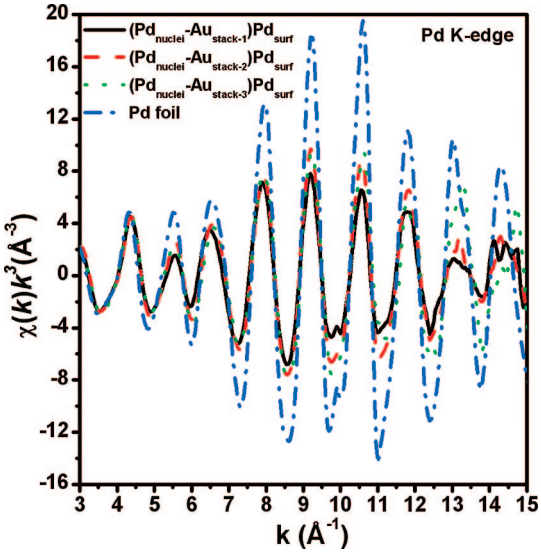

Figure 5. k^3-weighted EXAFS spectra recorded for Pd–Au bimetallic clusters with various atomic stackings at the Pd K-edge.

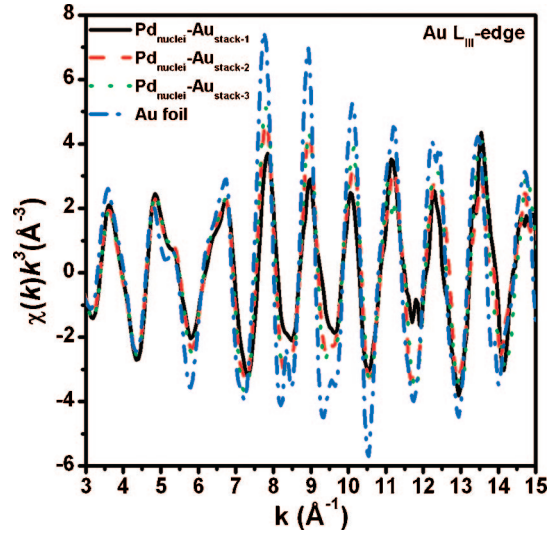

Figure 6. k^3-weighted EXAFS spectra recorded for Pd–Au bimetallic clusters with various atomic stackings at the Au L_{III}-edge.

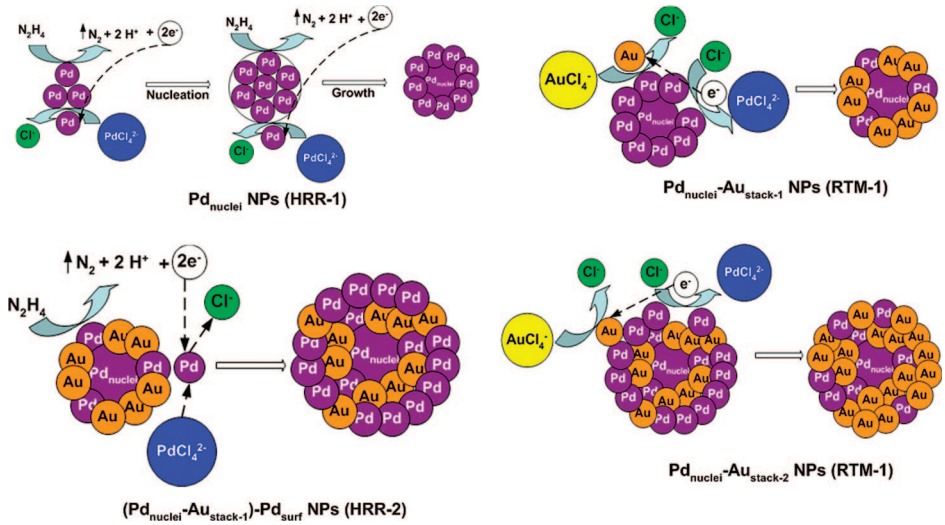

Scheme 1. Schematic of the architecture of Pd–Au bimetallic NPs in AOT reverse microemulsions.

standard reduction potential of the reaction $AuCl_4^- + 3e^- \rightarrow Au + 4Cl^-$ (1.008 V vs SHE) is greater than that of $PdCl_4^{2-} + 2e^- \rightarrow Pd + 4Cl^-$ (0.591 V vs SHE).[44] Hence, the $AuCl_4^-$ ions in the solutions can be reduced only *via* the RTM between Pd^0 clusters and Au^{3+} ions, and the electron required for the reduction is contributed from the oxidation of Pd^0 to Pd^{2+}. The direct reduction of Au^{3+} ions to Au^0 by the oxidation of Pd^0 to Pd^{2+} without any ligand exchange effect can be further seen in the FT k^3-weighted EXAFS spectral features at the Au L_{III}-edge and the Pd K-edge of the Pd–Au bimetallic NPs which are formed by mixing equal numbers of moles of Pd clusters and $AuCl_4^-$ precursor, $N_{Au}/N_{Pd} = 1$ (see Figure 4S, Supporting Information). Two peaks corresponding to the Pd–Cl and Pd–M coordination in the Pd K-edge spectra and the Au–M coordination in the Au L_{III}-edge spectra are observed after the addition of an equal number of moles of $AuCl_4^-$ precursor to the Pd clusters (Figure 4S, Supporting Information). In our previous study regarding the formation of bimetallic Ag–Pd NPs, the $PdCl_4^{2-}$ ions were directly reduced by monometallic Ag NPs *via* the RTM, and the electron required for the reduction was contributed from the direct oxidation of Ag^0 to Ag^+.[32] We also studied the formation mechanism of both monometallic Pt[31] and bimetallic Pd–Pt NPs[33] in AOT reverse micelles. It was found that the reduction of $PtCl_6^{2-}$ is not a direct one, and it involves three steps. The electrons obtained from the oxidation of Pd^0 to $PdCl_4^{2-}$ species cannot be used to produce a Pt layer on the Pd clusters directly,[33] indicating that the $PtCl_6^{2-}$ species are not appropriate candidates for producing Pd_{core}–Pt_{shell}-type NPs *via* the RTM. However, in the present study, the reduction of $AuCl_4^-$ species is a direct one, suggesting that $AuCl_4^-$ is a good candidate for controlling the shell layer and further modifying the electronic structure and alloying extent of the bimetallic NPs.

HRR-2. After the first RTM, the dosage of N_2H_5OH is increased to 79.2×10^{-5} mol at 6.8 h. At this stage, there is a complete absence of Pd–Cl coordination, and N_{Pd-Pd} and N_{Pd-Au} are found to be increased to 6.37 and 0.87, respectively. Also, N_{Au-Pd} and N_{Au-Au} are found to be 1.37 and 8.17, respectively. These results suggest that $PdCl_4^{2-}$ species are completely reduced back to Pd^0 and deposited on the Pd_{nuclei}–$Au_{stack-1}$ NPs, thereby producing (Pd_{nuclei}–$Au_{stack-1}$)–Pd_{surf} NPs (**HRR-2**, Scheme 1). One can control the surface composition of Pd and Au on the NPs by properly adjusting the molar ratio of Au^{3+} ions and Pd^{2+} ions in the solution before performing HRRs.

RTM-2. Later, when $AuCl_4^-$ is added with an N_{Au}/N_{Pd} stoichiometric ratio of 0.862 at 8.6 h to the solution containing (Pd_{nuclei}–$Au_{stack-1}$)–Pd_{surf} NPs obtained from HRR-2, N_{Pd-Pd} and N_{Pd-Au} are decreased to 2.59 and 0.24, respectively, and N_{Pd-Cl} is increased to 2.53. These results indicate that surface Pd atoms from (Pd_{nuclei}–$Au_{stack-1}$)–Pd_{surf} stacked NPs are dissolved again and transformed to the $PdCl_4^{2-}$ species. The Au^{3+} ions are reduced to Au^0 to form Pd_{nuclei}–$Au_{stack-2}$ with a second Au stacking (**RTM-2**, Scheme 1). The increase in coordination N_{Au-Au} at this stage to 8.45 indicates that the thickness of Au stacking can be controlled by properly employing the Au precursor solution.

HRR-3. The $PdCl_4^{2-}$ species generated in the above step are further reduced to Pd^0 after increasing the dosage of N_2H_5OH to 96.8×10^{-5} mol at 10.4 h. N_{Pd-Pd} and N_{Pd-Au} are increased to 6.46 and 1.06, respectively, and the absence of Pd–Cl coordination is observed. These results suggest that the Pd^0 clusters are deposited on the surface of Pd_{nuclei}–$Au_{stack-2}$ NPs to produce (Pd_{nuclei}–$Au_{stack-2}$)–Pd_{surf} NPs.

RTM-3. When Au precursor solution is again introduced into the microemulsion system containing (Pd_{nuclei}–$Au_{stack-2}$)–Pd_{surf} NPs formed in the step HRR-3,

TABLE 3. Structural Coordination Number Parameters and Alloying Extent of Au and Pd for Different Atomic Ratios, N_{Au}/N_{Pd}, of Pd–Au Bimetallic Clusters with Various Atomic Stackings

system	molar ratio (N_{Au}/N_{Pd})	A ($=\sum N_{Au\text{-}i}$)	B ($=\sum N_{Pd\text{-}i}$)	$P_{observed}$	$R_{observed}$	P_{random}	R_{random}	J_{Au} (%)	J_{Pd} (%)
$(Pd_{nuclei}–Au_{stack\text{-}1})–Pd_{surf}$ NPs	0.633	9.54	7.24	0.14	0.12	0.61	0.39	22.9	30.8
$(Pd_{nuclei}–Au_{stack\text{-}2})–Pd_{surf}$ NPs	0.862	9.70	7.52	0.13	0.14	0.54	0.46	24.1	30.4
$(Pd_{nuclei}–Au_{stack\text{-}3})–Pd_{surf}$ NPs	0.997	10.30	6.76	0.11	0.16	0.50	0.50	22.0	32.0

with an N_{Au}/N_{Pd} stoichiometric ratio of 0.997 at 14.7 h, N_{Pd-Cl}, N_{Pd-Pd}, and N_{Pd-Au} are found to be 1.96, 1.81, and 0.21, respectively, and N_{Au-Au} is increased to 9.20, which corresponds to the formation of $Pd_{nuclei}–Au_{stack\text{-}3}$ NPs. This observation is similar to what is observed during the formation of $Pd_{nuclei}–Au_{stack\text{-}1}$ and $Pd_{nuclei}–Au_{stack\text{-}2}$ NPs, *i.e.*, the occurrence of a replacement reaction between the shell Pd^0 clusters and added Au^{3+} ions, except that the increased N_{Au-Au} value suggests the increased thickness of Au stacking.

HRR-4. Finally, the dosage of N_2H_5OH is increased to 110.5×10^{-5} mol at 16.5 h in the microemulsion system containing $Pd_{nuclei}–Au_{stack\text{-}3}$ NPs formed in the step HRR-3. N_{Pd-Au} and N_{Pd-Pd} are found to be 5.67 and 1.09, respectively. The complete absence of Pd–Cl coordination indicates that all $PdCl_4^{2-}$ species are completely reduced to form $(Pd_{nuclei}–Au_{stack\text{-}3})–Pd_{surf}$ NPs.

Pd and Au Atomic Distribution and Alloying Extent in $(Pd_{nuclei}–Au_{stack})–Pd_{surf}$ Stacked Bimetallic Nanoparticles. The atomic distribution and alloying extent of Pd and Au in $(Pd_{nuclei}–Au_{stack})–Pd_{surf}$ stacked bimetallic NPs are obtained by employing our previously developed XAS methodology.[20] In the case of $(Pd_{nuclei}–Au_{stack\text{-}1})–Pd_{surf}$ stacked Pd–Au bimetallic NPs formed during the second HRR, N_{Au-Au} and N_{Au-Pd} are determined as 8.17 and 1.37, respectively, giving the total coordination number of Au and Pd around Au, A ($=\sum N_{Au\text{-}i} = N_{Au-Au} + N_{Au-Pd}$), as 9.54. Similarly, N_{Pd-Pd} and N_{Pd-Au} are determined as 6.37 and 0.87, respectively, providing the total coordination number of Pd and Au around Pd, B ($=\sum N_{Pd\text{-}i} = N_{Pd-Pd} + N_{Pd-Au}$), as 7.24. From these values, the structural parameters $P_{observed}$ ($= N_{Au-Pd}/\sum N_{Au\text{-}i}$) and $R_{observed}$ ($= N_{Pd-Au}/\sum N_{Pd\text{-}i}$) are calculated as 0.14 and 0.12, respectively. The $P_{observed}$ and $R_{observed}$ values can be used to describe the atomic distribution of Au and Pd, respectively, in Pd–Au bimetallic NPs. The alloying extent of Au (J_{Au}) and Pd (J_{Pd}) can be estimated from the $P_{observed}$ and $R_{observed}$ values by employing eqs 2 and 3, respectively.

$$J_{Au} = \frac{P_{observed}}{P_{random}} \times 100\ (\%) \qquad (2)$$

$$J_{Pd} = \frac{R_{observed}}{R_{random}} \times 100\ (\%) \qquad (3)$$

P_{random} and R_{random} can be taken as 0.5 if the atomic ratio of Au to Pd is 1:1. However, at HRR-2, the atomic ratio of Au to Pd is calculated as 0.633:1. From this ratio, P_{random} and R_{random} can be taken as 0.61 and 0.39, respectively. By substituting these values into eqs 2 and 3, J_{Au} and J_{Pd} are calculated as 22.9% and 30.8%, respectively. The higher J_{Pd} value indicates a higher degree of alloying around Pd atoms and less segregation of Pd. In contrast, the lower J_{Au} value suggests a lower degree of alloying around Au atoms and more segregation of Au. The J_{Au} and J_{Pd} values, along with other structural parameters, for NPs obtained at different reaction states, *i.e.*, $(Pd_{nuclei}–Au_{stack\text{-}1})–Pd_{surf}$, $(Pd_{nuclei}–Au_{stack\text{-}2})–Pd_{surf}$, and $(Pd_{nuclei}–Au_{stack\text{-}3})–Pd_{surf}$ NPs, are listed in Table 3. The similarity in J_{Au} and J_{Pd} values obtained for different reaction states indicates that the Pd–Au bimetallic NPs produced at these reaction states are similar in structure.

For a homogeneous bimetallic $P_{core}–R_{shell}$ cluster ($N_P/N_R = 1$), for which the core of the cluster is composed of N_P atoms of P and the surface is made of N_R atoms of R, the total coordination ($N_{P\text{-}P} + N_{P\text{-}R}$) is equal to 12 for the P atom and less than 12 for the R atom.[45] If the total coordination number ($N_{P\text{-}P} + N_{P\text{-}R}$) is much lower than 12, most of the P atoms are dispersed on the cluster surface. It is very interesting that the total coordination number of Au, A ($=\sum N_{Au\text{-}i} = N_{Au-Au} + N_{Au-Pd}$), gradually increases with the increase in N_{Au}/N_{Pd}, indicating that most of the Au atoms are occupied in the core region and only a few Au atoms are dispersed on the cluster surface. However, the total coordination number of Pd, B ($=\sum N_{Pd\text{-}i} = N_{Pd-Pd} + N_{Pd-Au}$) is decreased to 6.76 for $(Pd_{nuclei}–Au_{stack\text{-}3})–Pd_{surf}$ NPs, indicating that most of the Pd atoms are dispersed on the cluster surface. This result is consistent with the UV–vis absorption spectral features shown in Figure 7. As can be seen from Figure 7, the surface plasmon absorption band of the $(Pd_{nuclei}–Au_{stack\text{-}3})–Pd_{surf}$ NPs is much lower than that of the pure Au clusters and closer to that of the pure Pd clusters, indicating that the surface of the Pd–Au bimetallic NPs obtained in this work has more Pd atoms than the inner core. Both XAS and UV–vis observations show that the Pd–Au bimetallic NPs follow $(Pd_{nuclei}–Au_{stack})–Pd_{surf}$ stacking, and only a few Au atoms are dispersed on the catalyst surface.

A HRTEM image of $(Pd_{nuclei}–Au_{stack\text{-}3})–Pd_{surf}$ NPs is shown in Figure 8. The image shows that the size distribution of the clusters is monodisperse. The particle size of clusters obtained from the TEM image, about 2.5–3.0 nm, is slightly larger than that obtained from XAS analysis (*ca.* 2.5 nm). This may happen due to the aggregation of particles caused by the drying process

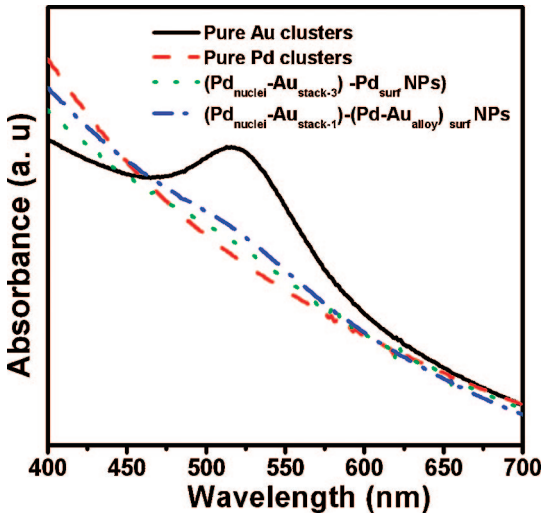

Figure 7. UV–vis spectra of pure Au, Pd, (Pd$_{nuclei}$–Au$_{stack-3}$)–Pd$_{surf}$, and (Pd$_{nuclei}$–Au$_{stack-1}$)–(Pd–Au$_{alloy}$)$_{surf}$ NPs.

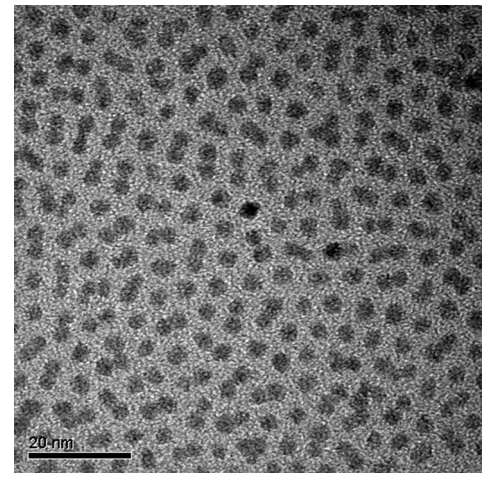

Figure 8. HRTEM image of the (Pd$_{nuclei}$–Au$_{stack-3}$)–Pd$_{surf}$ NPs in AOT reverse microemulsions.

before HRTEM analysis. Our previous studies on Pt formation in AOT reverse micelles too indicated that the particle size obtained from TEM is larger than that obtained from XAS analysis.[31]

In order to check the applicability of the present design methodology, a bimetallic (Pd–Au)$_{alloy}$ cluster with a (Pd$_{nuclei}$–Au$_{stack-1}$)–(Pd–Au$_{alloy}$)$_{surf}$ stacking was synthesized. At first the Au^{3+} ions with $N_{Au}/N_{Pd} = 1$ were added to the preformed Pd$_{nuclei}$ cluster. The RTM between Pd$_{nuclei}$ clusters and the Au^{3+} ions generated Pd$_{nuclei}$–Au$_{stack-1}$ NPs, leaving $PdCl_4^{2-}$ and residual $AuCl_4^-$ species. The general idea in adding excess Au precursor to the Pd$_{nuclei}$ clusters is to control the insufficient amount of the electron donated by the surface Pd atoms of the Pd$_{nuclei}$ clusters required for the reduction of Au precursor. In the corresponding k^3-weighted EXAFS spectra at the Au L_{III}-edge and at the Pd K-edge, two peaks were observed, corresponding to the coordination of Pd–Cl and Pd–M (in Pd K-edge EXAFS spectra) and the coordination of Au–Cl and Au–M (in Au L_{III}-edge EXAFS spectra) (see Figure 4S, Supporting Information). Later, in order to make a (Pd–Au)$_{alloy}$ layer on the surface of Pd$_{nuclei}$–Au$_{stack-1}$ NPs, HRR was performed by adding 110×10^{-5} mol of N_2H_5OH into the microemulsion system to allow the co-reduction of both the Pd^{2+} and Au^{3+} ions. At this stage, the Pd–M bond at the Pd K-edge and the Au–M bond at the Au L_{III}-edge were split into two peaks, located between 2.0 and 3.0 Å, and both the Pd–Cl and Au–Cl bonds disappeared. These results indicate that the cluster possesses an atomic distribution in the shell region different from that of the (Pd$_{nuclei}$–Au$_{stack}$)–Pd$_{surf}$ stacked bimetallic NPs. The fitting of the (Pd$_{nuclei}$–Au$_{stack-1}$)–(Pd–Au$_{alloy}$)$_{surf}$ NPs at the Pd K-edge and the Au L_{III}-edge, as shown in Tables 1 and 2, respectively, indicates that the two peaks at the Pd K-edge correspond to the Pd–Pd and Pd–Au bonds, and the two peaks at the Au L_{III}-edge correspond to the Au–Pd and Au–Au bonds. Here, too, the Pd–Pd and Pd–Au bonds at the Pd K-edge, and the Au–Pd and Au–Au bonds at the Au L_{III}-edge, are reliable as realized from the close matching of the two-shell theoretical fit with that of the back-transformed experimental spectra (see Figure 5S, Supporting Information). The composition of the designed (Pd$_{nuclei}$–Au$_{stack-1}$)–(Pd–Au$_{alloy}$)$_{surf}$ NPs is calculated from XAS by measuring the edge jump at both the Pd K-edge and the Au L_{III}-edge, and N_{Au}/N_{Pd} is found to be 1.00. N_{Au-Au} and N_{Au-Pd} are found to be 6.41 and 4.12, respectively and the total coordination number, A ($= N_{Au-i}$), is 10.53. N_{Pd-Pd} and N_{Pd-Au} are found to be 1.91 and 4.12, respectively, and the total coordination number, B ($= N_{Pd-i}$), is 6.03. By using eqs 2 and 3, J_{Au} and J_{Pd} are calculated as 78.0% and 136%, respectively. The J_{Au} and J_{Pd} values of (Pd$_{nuclei}$–Au$_{stack-1}$)–(Pd–Au$_{alloy}$)$_{surf}$ NPs show an increasing trend when compared to the J_{Au} and J_{Pd} values of (Pd$_{nuclei}$–Au$_{stack-1\ to\ 3}$)–Pd$_{surf}$ NPs. We believe that the co-reduction of Pd^{2+} and Au^{3+} ions generates a higher population of alloyed Pd and Au and thereby increases J_{Au} and J_{Pd}. That $J_{Pd} > 100\%$ and $J_{Au} < 100\%$ indicates that the "Au" atoms prefer "Au" rather than "Pd" and the "Pd" atoms prefer "Au" rather than "Pd", and as an average result, the atomic distribution of the Pd atoms is better than that of the Au atoms. The UV–vis spectra shown in Figure 7 show that the surface plasmon absorption band of the (Pd$_{nuclei}$–Au$_{stack-1}$)–(Pd–Au$_{alloy}$)$_{surf}$ NPs is slightly higher than that of the Pd–Au bimetallic clusters, indicating that the surface is made of a Pd–Au alloy layer. This observation indicates that (Pd$_{nuclei}$–Au$_{stack-1}$)–(PdAu$_{alloy}$)$_{surf}$ NPs can be successfully built by modifying the surface of Pd$_{nuclei}$–Au$_{stack-1}$ stacked bimetallic NPs and further supports the possibility of controlling the surface composition of Pd and Au in the cluster. In the resultant cluster, Au atoms are rich in the core region, alloyed Pd–Au atoms are preferentially located on the surface with a higher atomic distribution of Pd, and Pd atoms act as nuclei to form (Pd$_{nuclei}$–Au$_{stack-1}$)–(Pd–Au$_{alloy}$)$_{surf}$ NPs. The effective control of the RTMs and HRRs can really offer the design and construction of bimetallic clusters with controlled properties in microemulsions. The present XAS methodology can be easily extended to control the alloying extent, atomic distribution, atomic stacking, and electronic structure of other bimetallic NP systems.

CONCLUSION

We have successfully designed and controlled the nucleation and growth of Pd–Au bimetallic NPs with a (Pd_{nuclei}–Au_{stack})–Pd_{surf} stacking within AOT reverse microemulsions as monitored by *in situ* XAS. The overall architecture of Pd–Au bimetallic NPs was reasonably explained on the basis of the *in situ* XAS observations. We have demonstrated that, by properly employing the redox transmetalation reaction with a controlled amount of Au precursor solution, the Au stacking in Pd–Au bimetallic NPs can be tuned. In addition, we demonstrated that the surface of Pd_{nuclei}–$Au_{stack\text{-}1}$ NPs can be modified by either Pd or Pd–Au_{alloy}, by employing appropriate hydrazine reduction and redox transmetalation reactions, to generate (Pd_{nuclei}–$Au_{stack\text{-}1}$)–Pd_{surf} and (Pd_{nuclei}–$Au_{stack\text{-}1}$)–(Pd–Au_{alloy})$_{surf}$ stacked NPs, respectively. We believe that the surface composition of Pd and Au in Pd–Au bimetallic NPs can be controlled by properly employing hydrazine, Pd, and Au precursor solutions. This is of considerable importance, since the sizeable (Pd–Au_{alloy})$_{surf}$ may impart superior catalytic properties to (Pd_{nuclei}–$Au_{stack\text{-}1}$)–(Pd–Au_{alloy})$_{surf}$ NPs when compared to the Pd_{nuclei}–$Au_{stack\text{-}1}$ and (Pd_{nuclei}–$Au_{stack\text{-}1}$)–Pd_{surf} stacked NPs. The Pd–Au NPs with variable Au stacking and sizeable surface Pd and Au populations may be found useful for catalytic applications. Our ongoing work is aimed at modifying the Pd_{surf} layer of (Pd_{nuclei}–$Au_{stack\text{-}1}$)–Pd_{surf} stacked bimetallic Pd–Au NPs systematically with the other possible metals, to generate other bimetallic systems for interesting applications, and investigating their structures by the described XAS methodology.

EXPERIMENTAL SECTION

Synthesis of Nanoparticles in AOT Reverse Micelles. ***Pd_{nuclei} Nanoparticles via Hydrazine Reduction Reaction 1 (HRR-1).*** The monometallic Pd_{nuclei} clusters, used as both templates and seeds in further reactions, were prepared in the microemulsion solution containing *n*-heptane as the continuous oil component, water, and surfactant. The surfactant used was 1 M sodium bis(2-ethylhexyl)sulfosuccinate (AOT) (99%). The *n*-heptane and the surfactant were thoroughly mixed, and an aqueous solution of 0.82 mL of 0.5 M K_2PdCl_4 was subsequently added to form a well-defined microemulsion phase with Pd complex in the water pool. The volume ratio of an aqueous phase to an organic phase was kept at 1:10. An important parameter characterizing the microemulsion, *i.e.*, the water-to-surfactant molar ratio, W_0 {(water)/(surfactant)}, was equal to 5.5 in the present experiment. This microemulsion solution was placed in the liquid cell, which was carefully designed governing the edge jump, for the *in situ* XAS measurement. A microemulsion of the same composition of oil, water, and the surfactant that contained the reducing agent was also prepared. The reducing agent solution was composed of 1 M hydrazine (N_2H_5OH). To control the particle size of the Pd clusters, an appropriate amount of reducing agent containing microemulsion was then gradually added to the microemulsion containing Pd complex using a microsyringe each hour, starting from 1 and going to 4.5 h, whereby the Pd complex was reduced to Pd^0 clusters.

(Pd_{nuclei}–$Au_{stack\text{-}1}$) Nanoparticles via Redox Transmetalation Reaction 1 (RTM-1). To the microemulsion containing Pd_{nuclei} clusters was introduced the Au precursor solution, *i.e.*, the $HAuCl_4$ emulsion, which was prepared by using a procedure similar to that used for the preparation of the K_2PdCl_4 microemulsion, at 5.5 h with a N_{Au}/N_{Pd} ratio kept at 0.633 to allow the first RTM between Pd_{nuclei} clusters and the added Au^{3+} ions. In this reaction, part of the Pd from the preformed Pd_{nuclei} clusters was oxidized to Pd^{2+}, and Au^{3+} ions were reduced on Pd_{nuclei} clusters, producing Pd–Au bimetallic NPs with a first atomic stacking (Pd_{nuclei}–$Au_{stack\text{-}1}$).

(Pd_{nuclei}–$Au_{stack\text{-}1}$)–Pd_{surf} Nanoparticles via Hydrazine Reduction Reaction 2 (HRR-2). To the solution obtained in step RTM-1, containing Pd_{nuclei}–$Au_{stack\text{-}1}$ NPs and Pd^{2+} ions, the dosage of hydrazine was increased to 79.2×10^{-5} mol at 6.8 h in order to perform a HRR. The Pd^{2+} ions in the microemulsion solution were reduced back to Pd on the surface of the Pd_{nuclei}–$Au_{stack\text{-}1}$ NPs, and (Pd_{nuclei}–$Au_{stack\text{-}1}$)–Pd_{surf} stacked NPs were formed.

(Pd_{nuclei}–$Au_{stack\text{-}2}$) Nanoparticles via Redox Transmetalation Reaction 2 (RTM-2). Au^{3+} ions with an N_{Au}/N_{Pd} ratio of 0.862 were added at 8.6 h into the solution obtained in step HRR-2, containing the (Pd_{nuclei}–$Au_{stack\text{-}1}$)–Pd_{surf} NPs. The Pd_{nuclei}–$Au_{stack\text{-}2}$ NPs were produced *via* the RTM between Pd_{surf} particles and Au^{3+} ions. The thickness of the Au_{stack} layer of the Pd_{nuclei}–$Au_{stack\text{-}2}$ NPs was increased.

(Pd_{nuclei}–$Au_{stack\text{-}2}$)–Pd_{surf} Nanoparticles via Hydrazine Reduction Reaction 3 (HRR-3). Again we re-reduced the Pd^{2+} ions on the surface of Pd_{nuclei}–$Au_{stack\text{-}2}$ NPs formed in step RTM-2 by adding 96.8×10^{-5} mol of N_2H_5OH at 10.4 h to generate (Pd_{nuclei}–$Au_{stack\text{-}2}$)–Pd_{surf} NPs.

(Pd_{nuclei}–$Au_{stack\text{-}3}$) Nanoparticles via Redox Transmetalation Reaction 3 (RTM-3). To generate a third stacking of the Au layer, Au^{3+} ions were added with an N_{Au}/N_{Pd} ratio of 0.997 at 14.7 h to the solution obtained in step HRR-3, causing the RTM between the Pd_{surf} particles and Au^{3+} ions to take place to form Pd_{nuclei}–$Au_{stack\text{-}3}$ NPs with an increase in Au layer thickness.

(Pd_{nuclei}–$Au_{stack\text{-}3}$)–Pd_{surf} Nanoparticles via Hydrazine Reduction Reaction 4 (HRR-4). We further re-reduced the Pd^{2+} ions on the surface of Pd_{nuclei}–$Au_{stack\text{-}3}$ NPs formed at RTM-3 by adding 110×10^{-5} mol of N_2H_5OH at 16.5 h to generate (Pd_{nuclei}–$Au_{stack\text{-}3}$)–Pd_{surf} NPs.

The cycle of hydrazine reduction–redox transmetalation reactions can be continued to generate NPs with various atomic stackings. Meanwhile, the surface composition of NPs can be manipulated by carrying out the HRRs in the microemulsion solution containing a proper ratio of $Pd^{2+}$and Au^{3+} ions which can be added.

***In Situ* XAS Measurements.** The X-ray absorption spectra at the Pd K-edge and the Au L_{III}-edge were recorded at beamline BL12B2 at the Spring-8, Japan, and at beamline BL01C1 at the National Synchrotron Radiation Research Center, Hsinchu, Taiwan. For beamline BL12B2, the electron storage ring was operated at an energy of 8 GeV and a beam current of 100 mA. A double-crystal Si(111) monochromater was employed for energy selection, with a resolution $\Delta E/E$ better than 1×10^{-4} at both the Pd K-edge (24352 eV) and the Au L_{III}-edge (11917 eV). For beamline BL01C1, the electron storage ring was operated at 1.5 GeV with a beam current of 300 mA. BL01C1 utilizes the radiation from a superconducting wavelength shifter (E_c = 7.5 keV). The beamline employs a double-crystal Si(111) monochromator for energy selection, with a resolution $\Delta E/E$ better than 2×10^{-4} at both the Pd K-edge and the Au L_{III}-edge. Higher harmonics were eliminated by detuning double-crystal Si(111) by using a Rh-coated mirror at beamline BL12B2 or a Pt-coated mirror at beamline BL01C1. The formation of Pd_{nuclei} clusters and corresponding Pd–Au bimetallic clusters with various atomic stackings in reverse micelles was carried out in a home-made cell made of poly(tetrafluoroethylene) for *in situ* XAS study. Two holes were made in the cell, one on the top and the other on one side. After the liquid sample was added, the top hole was sealed with a Teflon rod to avoid exposing the sample to the atmosphere. A hollow Teflon rod with a Kapton film cap at one end was inserted into the side hole in the *in situ* cell. The position of the Teflon rod was adjusted to reach the optimum absorption thickness ($\Delta\mu x \approx 1.0$, where $\Delta\mu$ is the absorption edge and x is the thickness of the liquid layer) so that the proper edge-jump step

could be achieved during the measurements. All of the spectra were recorded at room temperature in transmission mode. Each reaction, from the initial state to the thermodynamically equivalent state, was monitored endlessly by X-ray absorption spectroscopy. Pd K-edge XAS spectra were recorded for all the hydrazine reduction reactions (HRR-1 to -4) and redox transmetalation reactions (RTM-1 to -3), whereas Au L_{III}-edge XAS spectra were recorded for all the redox transmetalation reaction steps (RTM-1 to -3) and for one hydrazine reduction reaction (HRR-2). All reactions were carried out at room temperature. Nitrogen gas was used to purge the microemulsion system throughout the experiment to prevent the clusters from being oxidized by air. The incident and transmission X-ray intensities were respectively detected by ion chambers that were installed in front of and behind the sample cell. Energy was scanned from 200 eV below the edge to 1000 eV above the edge. Standard reference compounds, Pd foil and Au foil for the respective edges, were measured simultaneously by using the third ionization chamber so that energy calibration could be performed scan by scan.

XAS Data Analysis. Standard procedures were followed to analyze the EXAFS data. First, the raw absorption spectrum in the pre-edge region was fitted to a straight line, and the background above the edge was fit using a 11-knot cubic spline function calculated from AUTOBK code. The EXAFS function, χ, was obtained by subtracting the post-edge background from the overall absorption and then normalizing with respect to the edge-jump step. The normalized $\chi(E)$ was transformed from energy space to k-space. The $\chi(k)$ data were weighted by k^3 in order to compensate for dampening of the XAFS amplitude with increasing k. Subsequently, k^3-weighted $\chi(k)$ data in the k-space ranging from 4.05 to 14.10 $Å^{-1}$ for the Pd K-edge and from 3.39 to 13.25 $Å^{-1}$ for the Au L_{III}-edge were Fourier transformed to r-space to separate the EXAFS contributions from different coordination shells. A nonlinear least-squares algorithm was applied to curve-fitting of EXAFS in r-space between 1.1 and 3.11 Å for the Pd K-edge and between 1.5 and 3.5 Å (without phase correction) for the Au L_{III}-edge. All the computer programs were implemented in the UWXAFS 3.0 package,[46] with the backscattering amplitude and the phase shift for the specific atom pairs being theoretically calculated by using FEFF7 code.[47] Palladium and gold foils were employed as references for the Pd–Pd and Au–Au bonds. Pd–Au and Au–Pd bonds are based on the face-centered-cubic (fcc) model containing six Pd and six Au atoms in symmetric positions. The amplitude reduction factor, S_0^2, for Au and Pd was obtained by analyzing the Au and Pd foils, respectively, and by fixing coordination numbers in the FEFFIT input file. The S_0^2 values are found to be 0.88 and 0.91 for Pd and Au, respectively.

HRTEM and Spectroscopic Analysis. High-resolution transmission electron microscopy measurements were carried out using a Phillips/FEI Tecnai 20 G2 S twin transmission electron microscope. The sample for HRTEM analysis was prepared by placing a drop of the dispersed solution onto a carbon-coated copper grid and allowing the solvent to be evaporated in a vacuum drybox at room temperature. All the UV absorption spectra were recorded on a Analytik Jena Specord-S 100 UV–vis spectrophotometer.

Acknowledgment. The authors gratefully acknowledge financial support from the National Science Council (NSC-95-2120-M-011-002 and NSC-95-2221-E-011-130) and facilities from the National Synchrotron Radiation Research Center (NSRRC), the National Taiwan University of Science and Technology, and the Institute of Atomic and Molecular Sciences, Academia Sinica, Taiwan.

Supporting Information Available: k^3-weighted EXAFS spectra of $(Pd–Au)_{alloy}$ clusters at both the Pd K-edge and the Au L_{III}-edge and their corresponding theoretical fit with back-transformed experimental data. This material is available free of charge *via* the Internet at http://pubs.acs.org.

REFERENCES AND NOTES

1. Nagabhushana, K. S.; Bönnemann, H. Wet chemical synthesis of nanoparticles. In *Nanotechnology in Catalysis*; Zhou, B., Hermans, S., Somorjai, G. A., Eds.; Kluwer Academic/Plenum Publishers: New York, 2004; pp 51–82.
2. Sun, S.; Murray, C. B.; Weller, D.; Folks, L.; Moser, A. Monodisperse FePt nanoparticles and ferromagnetic FePt nanocrystal superlattices. *Science* **2000**, *287*, 1989–1992.
3. Sinfelt, J. H. Structure of bimetallic clusters. *Acc. Chem. Res.* **1987**, *20*, 134–139.
4. Burch, R.; Garla, L. C. Platinum-tin reforming catalyst: II. Activity and selectivity in hydrocarbon reactions. *J. Catal.* **1981**, *71*, 360–372.
5. Shankar, S. S.; Rai, A.; Ahmad, A.; Sastry, M. J. Rapid synthesis of Au, Ag, and bimetallic Au core–Ag shell nanoparticles using Neem (*Azadirachta indica*) leaf broth. *J. Colloid Interface Sci.* **2004**, *275*, 496–502.
6. Damle, C.; Kumar, A.; Sastry, M. Synthesis of Ag/Pd Nanoparticles and Their Low Temperature Alloying within Thermally Evaporated Fatty Acid Films. *J. Phys. Chem. B* **2002**, *106*, 297–302.
7. Dounda, C. M.; Bertino, M. F.; Blum, F. D.; Tokuhiro, A. T.; Lahiridey, D.; Chattopadhyay, S.; Terry, J. Radiolytic Synthesis of Bimetallic Ag-Pt Nanoparticles with a High Aspect Ratio. *J. Phys. Chem. B* **2003**, *107*, 2966–2970.
8. Kumar, D.; Chen, M. S.; Goodman, D. W. Synthesis of vinyl acetate on Pd-based catalysts. *Catal. Today* **2007**, *123*, 77–85.
9. Crathorne, E. A.; MacGowan, D.; Morris, S. R.; Rawlinson, A. P. Application of isotopic transient kinetics to vinyl acetate catalysis. *J. Catal.* **1994**, *149*, 254–267.
10. Han, Y.-F.; Wang, J.-H.; Kumar, D.; Yan, Z.; Coodman, D. W. A kinetic study of vinyl acetate synthesis over Pd-based catalysts: kinetics of vinyl acetate synthesis over Pd–Au/SiO_2 and Pd/SiO_2 catalysts. *J. Catal.* **2005**, *232*, 467–475.
11. Venezia, A. M.; La Parola, V.; Nicoli, V.; Deganello, G. Effect of gold on the HDS activity of supported palladium catalysts. *J. Catal.* **2002**, *212*, 56–62.
12. Choudhary, T. V.; Sivadinarayana, C.; Datye, A. K.; Kumar, D.; Goodman, D. W. Acetylene hydrogenation on Au-based catalysts. *Catal. Lett.* **2003**, *86*, 1–8.
13. Enache, D. I.; Edwards, J. K.; Landon, P.; Solsona-Espriu, B.; Carley, A. F.; Herzing, A. A.; Watanabe, M.; Kiely, C. J.; Knight, D. W.; Hutchings, G. J. Solvent-free oxidation of primary alcohols to aldehydes using Au–Pd/TiO_2 catalysts. *Science* **2006**, *311*, 362–365.
14. Mizukoshi, Y.; Fujimoto, T.; Nagata, Y.; Oshima, R.; Maeda, Y. Characterization and catalytic activity of core–shell structured gold/palladium bimetallic nanoparticles synthesized by the sonochemical method. *J. Phys. Chem. B* **2000**, *104*, 6028–6032.
15. Wu, M.; Mao, G.; Meng, M. Preparation and characterization of the polymer-protected palladium-gold colloidal bimetallic catalysts. *J. Mol. Catal.* **1992**, *74*, 275–284.
16. Schmid, G.; Lehnert, A.; Malm, J.-O.; Bovin, J.-O. Ligand-stabilized bimetallic colloids identified by HRTEM and EDX. *Angew. Chem., Int. Ed. Engl.* **1991**, *30*, 874–876.
17. Harpeness, R.; Gedanken, A. Microwave synthesis of core–shell gold/palladium bimetallic nanoparticles. *Langmuir* **2004**, *20*, 3431–3434.
18. Scctt, R. W. J.; Wilson, O. M.; Oh, S. K.; Kenik, E. A.; Crooks, R. M. Bimetallic palladium–gold dendrimer-encapsulated catalysts. *J. Am. Chem. Soc.* **2004**, *126*, 15583–15591.
19. Kan, C.; Cai, Y.; Li, C.; Zhang, L.; Hofmeister, H. Ultrasonic synthesis and optical properties of Au/Pd bimetallic nanoparticles in ethylene glycol. *J. Phys. D: Appl. Phys.* **2003**, *36*, 1609–1614.
20. Hwang, B.-J.; Sarma, L. S.; Chen, J.-M.; Chen, C.-H.; Shih, S.-C.; Wang, G.-R.; Liu, D.-G.; Lee, J.-F.; Tang, M.-T. Structural models and atomic distribution of bimetallic nanoparticles as investigated by X-ray absorption spectroscopy. *J. Am. Chem. Soc.* **2005**, *127*, 11140–11145.
21. Bazin, D.; Guczi, L.; Lynch, J. Anomalous wide angle X-ray scattering (AWAXS) and heterogeneous catalysts. *Appl. Catal. A: Gen* **2002**, *226*, 87–113.
22. Iwasawa, Y. *X-ray absorption spectroscopy for catalysts and surfaces*; World Scientific: Singapore, 1996.
23. Grundwaldt, J. D.; Caravati, M.; Hannemann, S.; Baiker, A. X-ray absorption spectroscopy under reaction conditions: suitability of different reaction cells for combined catalyst

characterization and time-resolved studies. *Phys. Chem. Chem. Phys.* **2004**, *6*, 3037–3047.
24. Bazin, D.; Rehr, J. J. Limits and advantages of X-ray absorption near edge structure for nanometer scale metallic clusters. *J. Phys. Chem. B* **2003**, *107*, 12398–12402.
25. Bazin, D.; Sayers, D.; Rehr, J. J.; Mottet, C. Numerical simulation of the platinum L_{III} edge white line relative to nanometer scale clusters. *J. Phys. Chem. B* **1997**, *101*, 5332–5336.
26. Frenkel, A. I.; Hills, C. W.; Nuzzo, R. G. A view from inside: Complexity in the atomic scale ordering of supported metal nanoparticles. *J. Phys. Chem. B* **2001**, *105*, 12689–12703.
27. Nitani, H.; Nakagawa, T.; Daimon, H.; Kurobe, Y.; Ono, T.; Honda, Y.; Koizumi, A.; Seino, S.; Yamamoto, T. Methanol oxidation catalysis and substructure of PtRu bimetallic nanoparticles. *Appl. Catal. A: Gen.* **2007**, *326*, 194–201.
28. Sinfelt, J. H.; Via, G. H.; Lytle, F. W. Application of EXAFS in catalysis. Structure of bimetallic cluster catalysts. *Catal. Rev. Sci. Eng.* **1984**, *26*, 81–140.
29. Bazin, D. C.; Sayers, D. A.; Rehr, J. J. Comparison between X-ray absorption spectroscopy, anomalous wide angle X-ray scattering, anomalous small angle X-ray scattering, and diffraction anomalous fine structure techniques applied to nanometer-scale metallic clusters. *J. Phys. Chem. B* **1997**, *101*, 11040–11050.
30. Hwang, B.-J.; Tsai, Y.-W.; Sarma, L. S.; Tseng, Y. L.; Liu, D. G.; Lee, J. F. Genesis of bimetallic Pt–Cu clusters in reverse micelles investigated by in situ X-ray absorption spectroscopy. *J. Phys. Chem. B* **2004**, *108*, 20427–20434.
31. Tsai, Y.-W.; Tseng, Y. L.; Sarma, L. S.; Liu, D.-G.; Lee, J.-F.; Hwang, B.-J. Genesis of Pt clusters in reverse micelles investigated by in situ X-ray absorption spectroscopy. *J. Phys. Chem. B* **2004**, *108*, 8148–8152.
32. Chen, C.-H.; Sarma, L. S.; Wang, G.-R.; Chen, J.-M.; Shih, S.-C.; Tang, M.-T.; Liu, D.-G.; Lee, J.-F.; Chen, J.-M.; Hwang, B.-J. Formation of bimetallic Ag–Pd nanoclusters via the reaction between Ag nanoclusters and Pd^{2+} ions. *J. Phys. Chem. B* **2006**, *110*, 10287–10295.
33. Chen, C.-H.; Hwang, B.-J.; Wang, G.-R.; Sarma, L. S.; Tang, M.-T.; Liu, D.-G.; Lee, J.-F. Nucleation and growth mechanism of Pd/Pt bimetallic clusters in sodium bis(2-ethylhexyl)sulfosuccinate (AOT) reverse micelles as studied by in situ X-ray absorption spectroscopy. *J. Phys. Chem. B* **2005**, *109*, 21566–21575.
34. Wang, D.-Y.; Chen, C.-H.; Yen, H.-C.; Lin, Y.-L.; Huang, P.-Y.; Hwang, B.-J.; Chen, C.-C. Chemical transformation from FePt to $Fe_{1-x}PtM_x$ (M = Ru, Ni, Sn) nanocrystal by a cation redox reaction: X-ray absorption spectroscopic studies. *J. Am. Chem. Soc.* **2007**, *129*, 1538–1540.
35. Lee, W.-R.; Kim, M. G.; Cho, J.-R.; Park, J.-I.; Ko, S. J.; Oh, S. J.; Cheon, J. Redox-transmetallation process as a generalized synthetic strategy for core–shell magnetic nanoparticles. *J. Am. Chem. Soc.* **2005**, *127*, 16090–16097.
36. Guo, X-C.; Madix, R. J. Oxygen-activated combustion of alkenes on the Pd (100) surface. *J. Am. Chem. Soc.* **1995**, *117*, 5523–5530.
37. Stuve, E. M.; Madix, R. J. Oxidation of ethylene on Pd (100): bonding of ethylene and scavenging of dehydrogenation fragments by surface oxygen. *Surf. Sci.* **1985**, *169*, 293–304.
38. Luo, K.; Yi, C.-W.; Axnanda, S; Goodman, D. W. Preparation and characterization of silica supported Au–Pd model catalysts. *J. Phys. Chem. B* **2005**, *109*, 23517–23522.
39. Choi, S. J.; Kang, S. K. Structural transformation of PdPt nanoparticles probed with X-ray absorption near edge structure spectroscopy. *Catal. Today* **2004**, *93–95*, 561–566.
40. Prins, R.; Koningsberger, D. C. Catalysis. In *X-Ray Absorption: Principles, Applications, Techniques of EXAFS, SEXAFS, and XANES*; Koningsberger, D. C., Prins, R., Eds.; Wiley: New York, 1988; p 362.
41. Materlik, M.; Muller, J. E.; Wilkins, J. W. L-edge absorption spectra of the rare earths: Assessment of the single-particle picture. *Phys. Rev. Lett.* **1983**, *50*, 267–270.
42. Hirai, T.; Sato, H.; Komasawa, I. Mechanism of formation of CdS and ZnS ultrafine particles in reverse micelles. *Ind. Eng. Chem. Res.* **1994**, *33*, 3262–3266.
43. Wu, M. L.; Chen, D. H.; Huang, T. C. Synthesis of Au/Pd bimetallic nanoparticles in reverse micelles. *Langmuir* **2001**, *17*, 3877–3883.
44. *CRC Hand Book of Chemistry and Physics*, 80th ed.; Lide, D. R., Ed.; CRC Press: Boca Raton, FL, 1999–2000; p 8.
45. Moonen, J.; Slot, J.; Lefferts, L.; Bazin, D.; Dexpert, H. The influence of polydispersity and inhomogenity on EXAFS of bimetallic catalysts. *Physica B* **1995**, *208–209*, 689–690.
46. Stern, E. A.; Newville, M.; Ravel, B.; Yacoby, Y.; Haskel, D. The UWXAFS analysis package: philosophy and details. *Physica B* **1995**, *208–209*, 117–120.
47. Zabinsky, S. I.; Rehr, J. J.; Anukodinov, A. L.; Albers, R. C.; Eller, M. J. Multiple-scattering calculations of x-ray absorption spectra. *Phys. Rev. B* **1995**, *52*, 2995–3009.